

A novel GPU-based sonar simulator for real-time applications

Abstract

Sonar simulation requires great computational effort due to the complexity of acoustic physics, [mainly when applied in the underwater environment](#). This fact turns the challenge of reproducing sensor data into a non-trivial task. On the other hand, simulation of sonar operation data allows to evaluate algorithms and control systems without going to the real underwater environment; that reduces the costs and risks of in-field experiments. This paper proposes a novel real-time underwater imaging sonar simulator, which uses the OpenGL shading language (GLSL) chain [on graphics processing unit \(GPU\)](#), and is able to simulate two main types of sonar sensors: mechanical scanning imaging sonars (MSIS) and [forward-looking](#) sonars (FLS). The virtual underwater simulation was conceived based on three frameworks: (i) OpenSceneGraph (OSG) reproduces the ocean visual effects, (ii) Gazebo deals with physics effects, and (iii) the Robot Construction Kit (Rock) controls the sonar in underwater environments. [The proposed sonar simulator exploits the rasterization pipeline in order to build](#) a matrix comprised of echo intensity, distance and angular distortion, being all calculated over objects shapes in the 3D rendered scene. Sonar-intrinsic speckle noise and object material properties are also considered as part of the acoustic image. Our evaluation demonstrated that the proposed method is able to operate with high frame rate, as well as realistic sonar image quality in different virtual underwater scenarios.

Key words: Simulated sensor data, sonar imaging, GPU-based processing, Robot Construction Kit (Rock), Underwater robotics.

1. Introduction

Simulation is an useful tool for designing and programming autonomous robot systems. That allows evaluating robot behavior, without dealing with physical hardware or decision-making algorithms and control systems in real-time trials, as well as costly and time-consuming field experiments.

When working with autonomous underwater vehicles (AUVs), simulation of facilities are specially relevant. AUVs usually demand expensive hardware and perform long-term data gathering operations, taking place in restrictive sites. As AUV does not need umbilical cable, and the underwater communication carries on by unreliable acoustic links, the robot should be able to make completely autonomous decisions, even with low-to-zero external assistance. While the analysis and interpretation of sensor data can be performed in a post-processing step, a real-time simulation is strongly needed for testing and evaluation of vehicle's motion response, avoiding involved risks on real world rides.

AUVs usually act below the photic zone, with high turbidity and huge light scattering. This makes the quality of image acquisition by optical devices limited by a short range, and also artificially illuminated and clear visibility conditions. To tackle with that limitations, high-frequency sonars have been used primarily on AUVs' navigation and perception systems. Acoustic waves emitted by sonars are significantly less affected by water attenuation, aiding operation at greater ranges even as low-to-zero visibility conditions, with a fast refresh rate. Although sonar devices usually solve the main shortcomings of optical sensors, they provide noisy data of lower resolution and more difficult interpretation.

By considering sonar benefits and singularities along with

the need to evaluate AUVs, recent works proposed ray tracing [1, 2, 3, 4, 5, 6] and tube tracing-based [7] techniques to simulate acoustic data with very accurate results, although having a high computational cost. Bell [1] proposed a simulator based on optical ray tracing for underwater side-scan sonar imagery; images were generated by acoustic signals represented by rays, which are repeatedly processed, forming a 2D-array. Coiras and Groen [2] used frequency-domain signal processing to produce synthetic aperture sonar frames; in that method, the acoustic image was created by computing the Fourier transform of the acoustic pulse used to insonify the scene. For forward-looking sonar simulations, Guériot and Sintes [7] introduce a volume-based approach of energy interacting with the scene, and collected by the receiving sonar; the sound propagation is defined by series of acoustic tubes, being always orthogonal to the current sonar view, where the reverberation and objects surface irregularities are also addressed. Saç *et al.* [3] described a sonar model by computing the ray tracing in frequency domain; when a ray hits an object in 3D space, three parameters are calculated to process the acoustic data: the Euclidean distance from the sonar axis, the intensity of returned signal by Lambert Illumination model and the surface normal; the reverberation and shadow phenomena are also considered in the scene rendering. DeMarco *et al.* [4] used Gazebo and Robot Operating System (ROS) [8] integration to simulate acoustic sound pulses by ray tracing technique, also producing a 3D point cloud of the coverage area; the reflected intensity has taken into account the object reflectivity, and the noise is applied in the sonar image by adding Gaussian and salt-and-pepper noises empirically defined. Gu *et al* [5] modeled a forward-looking device, where the ultrasound beams were formed by a set of rays; the acoustic image is significantly limited by its representation using only

64 two colors: white, when the ray strikes an object, and black for
 65 shadow areas. Kwak *et al.* [6] tried to improve the previous
 66 approach by adding a sound pressure attenuation to produce the
 67 gray-scale sonar frame, while the other physical characteristics
 68 related to sound transmission are disregarded.

69 1.1. Contributions

70 This paper introduces a novel imaging sonar simulator that
 71 presents some contributions when compared to the existing ap-
 72 proaches. Instead of simulating the sound pulse paths and the
 73 effects of their hits with the virtual objects, as presented by ray
 74 tracing and tube tracing-based methods [1, 2, 3, 4, 5, 6, 7], we
 75 take advantage of precomputed geometric data during the ras-
 76 terization pipeline to compute the acoustic frame. In addition,
 77 all raster data are handled on GPU, accelerating then the sim-
 78 ulation process with guarantee of real-time response, in con-
 79 trast to the methods found in [1, 2, 3, 4]. Although the mod-
 80 els found in [1, 2, 3, 4, 5, 6, 7], which address simulation of
 81 specific sonar device, our model is able to reproduce two kind
 82 of sonar devices: mechanical scanning imaging sonar (MSIS)
 83 and forward-looking sonar (FLS). The intensity measured back
 84 from the insonified objects depends on surface normal direc-
 85 tions and reflectivity, producing more realistic simulated frames
 86 than binary representation as found in [5, 6]. The speckle noise
 87 is modeled as a non-uniform Gaussian distribution and applied
 88 to the final sonar image, next to real sonar operation, differ-
 89 ently to [3, 4, 5, 6, 7]. **On the other hand, the additive noise is**
 90 **considered by the authors in [3, 4]. Finally, we have decided to**
 91 **extend the physical phenomena in the simulator, obeying the us-**
 92 **age in real-time experiments (e.g. decision-making algorithms**
 93 **and control system tuning). Knowing this real-time constraint,**
 94 **the high computational cost phenomena such as reverberation**
 95 **is not included at this point, differently of [3].**

96 The main goal here is to build quality and low time-con-
 97 suming acoustic frames, according to underwater sonar image
 98 formation and operation modes (see Section 2). **The shader ma-**
 99 **trix with depth, intensity and angular distortion parameters are**
 100 **extracted from underwater scene during the rasterization pipe-**
 101 **line, and subsequently fused to generate the simulated sonar**
 102 **data, as described in Section 3. Qualitative and time evalua-**
 103 **tion results for two different sonar devices are presented in Section**
 104 **4, allowing the use of the proposed simulator by real-time ap-**
 105 **plications.**

106 2. Imaging sonar operation

107 Sonars are echo-ranging devices that use acoustic energy to
 108 locate and survey objects in a desired area. The sonar trans-
 109 ducer emits pulses of sound waves (or ping) until they hit any
 110 object or be completely absorbed. When the acoustic signal
 111 collides with a surface, part of this energy is reflected, while
 112 other is refracted. The sonar data is built by plotting the echo
 113 measured back versus time of acoustic signal. The transducer
 114 reading in a given direction forms a *beam*. A single beam trans-
 115 mitted from a sonar is illustrated in Fig. 1. The horizontal and
 116 vertical beamwidths are represented by the azimuth ψ and el-
 117 evation θ angles, respectively, where each sampling along the

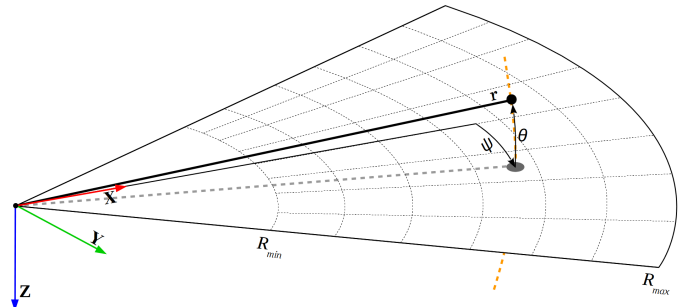


Figure 1: Imaging sonar geometry. By a projection process, all 3D points belonging to the same elevation arc (represented as dashed orange line) will be represented to the same image point in the 2D plane. Range r and azimuth angle ψ are measured, and elevation angle θ is lost. Sonar coverage area is defined by R_{min} and R_{max} .

118 beam is named as *bin*. The sonar coverage area is defined by
 119 R_{min} and R_{max} . Since the speed of sound underwater is known,
 120 or can be measured, the time delay between the emitted pulses
 121 and their echoes reveal how far the objects are (distance r), as
 122 well as how fast they are moving. The backscattered acoustic
 123 power in each bin determines the intensity value.

124 With different azimuth directions, the array of transducer
 125 readings forms the final sonar image. Since all incoming sig-
 126 nals converge to the same point, the reflected echoes could have
 127 been originated anywhere along the corresponding elevation arc
 128 at a fixed range, as depicted in Fig. 1. In the acoustic represen-
 129 tation, the 3D information is lost in the projection into a 2D
 130 image.

131 2.1. Sonar characteristics

132 Although sonar devices overcome main limitations of opti-
 133 cal sensors, they present more difficult data interpretation due
 134 to:

- 135 (a) **Shadowing:** This effect is caused by objects blocking the
 136 sound waves transmission and causing regions behind them,
 137 without acoustic feedback. These regions are defined by a
 138 black spot in the resulting sonar image;
- 139 (b) **Non-uniform resolution:** The amount of pixels used to
 140 represent an intensity record in the Cartesian coordinate
 141 system grows as its range increases. This fact causes im-
 142 age distortions and object flatness;
- 143 (c) **Changes in viewpoint:** Imaging the same scene from dif-
 144 ferent viewpoints can cause occlusions, shadows move-
 145 ments and significant changes of observable objects [9].
 146 For instance, when an outstanding object is insonified, its
 147 shadow is shorter, as the sonar becomes closer;
- 148 (d) **Low signal-to-noise ratio (SNR):** sonars suffer from low
 149 SNR mainly due the very-long-range scanning, and the
 150 presence of speckle noise introduced by acoustic wave in-
 151 terferences [10];
- 152 (e) **Reverberation:** This phenomenon is caused when mul-
 153 tiple acoustic waves, returning from the same object, are
 154 detected over the same ping, producing duplicated objects.

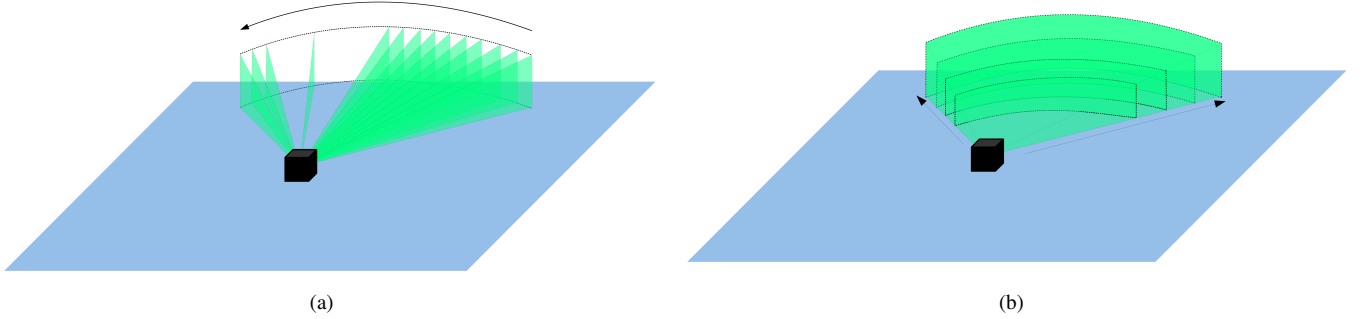


Figure 2: Different underwater sonar readings: (a) From a mechanical scanning imaging sonar and (b) from a forward-looking sonar.

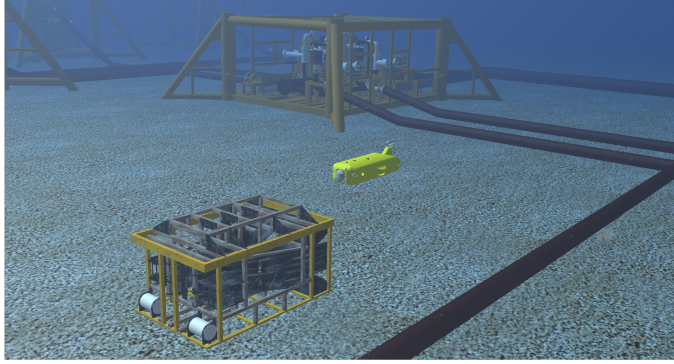


Figure 3: The AUV in Rock-Gazebo underwater scene.

155 2.2. Types of underwater sonar devices

156 The most common types of underwater acoustic sonars are
157 MSIS and FLS. In the former, the sonar image is built for each
158 pulse, with one beam per reading (see Fig. 2(a)); the resulting
159 sonar images in MSIS are usually depicted on a display pulse by
160 pulse, and the head position reader is rotated according to mo-
161 tor step angle. After a full 360° sector reading (or the desired
162 sector defined by left and right limit angles), the accumulated
163 sonar data is overwritten. The acquisition of a scanning image
164 involves a relatively long time, introducing distortions caused
165 by the vehicle movements. This sonar device is generally ap-
166 plied in obstacle avoidance [11] and navigation [12] applica-
167 tions. As illustrated in Fig. 2(b), the whole forward view of
168 an FLS is scanned and the current data is overwritten by the
169 next scanning in a high frame rate, with all beams being read
170 simultaneously; this is similar to a streaming video imagery for
171 real-time applications; this imaging sonar is commonly used
172 for navigation [13], mosaicing [9], target tracking [14] and 3D
173 reconstruction [15].

174 3. GPU-based sonar simulation

175 The goal of our work is to simulate the two types of under-
176 water sonar, discussed in Section 2.2, by vertex and fragment
177 processing and low computational cost. The complete pipeline
178 of the proposed simulator (from the virtual scene to the simu-
179 lated acoustic data) is detailed in the following sections. The

180 sonar simulator is written in C++ with OpenCV [16] support as
181 Rock packages.

182 3.1. Rendering underwater scene

183 In Rock-Gazebo framework [17], Gazebo handles with phys-
184 ical forces, while Rock's visualization tools are responsible by
185 the scene rendering. The graphical data in Rock are based
186 on OpenSceneGraph framework, an open source C/C++ 3D
187 graphics toolkit built on OpenGL. The osgOcean framework is
188 used to simulate the ocean visual effects, and the ocean buoy-
189 ancy is defined by the Gazebo, as described in [17]. In our case,
190 Rock-Gazebo integration provides the underwater scenario, al-
191 lowing also real-time hardware-in-the-loop simulation with a
192 virtual AUV.

193 All scene aspects, such as world model, robot parts (in-
194 cluding sensors and joints) and other objects presented in the
195 environment are defined by simulation description files (SDF),
196 which use the SDFormat [18], a XML format used to describe
197 simulated models and environments for Gazebo. Visual and
198 collision geometries of vehicle and sensor robot are also de-
199 scribed in specific file formats. Each component described in
200 the SDF file becomes a Rock component, which is based on
201 the Orococos real-time toolkit (RTT) [19], providing I/O ports,
202 properties and operations as communication layers. When the
203 models are loaded, Rock-Gazebo creates I/O ports to allow real
204 world or simulated system components interacting with the sim-
205 ulated models. A resulting scene sample of this integration is
206 illustrated in Fig. 3.

207 3.2. Sonar rendering

208 The rendering pipeline can be customized by defining GPU
209 shaders. A shader is written in OpenGL Shading Language
210 (GLSL) [20], a high-level language with a C-based syntax which
211 enables more direct control of graphics pipeline, which avoids
212 the use of low-level or hardware-specific languages. Shaders
213 can describe the characteristics of either a vertex or a fragment
214 (a single pixel). Vertex shaders are responsible by transform-
215 the vertex position into a screen position by the rasterizer, gen-
216 erating texture coordinates for texturing, and lighting the vertex
217 to determine each color. The rasterization results in a set of pix-
218 els to be processed by fragment shaders, which manipulate their
219 locations, depth and alpha values, and interpolated parameters
220 from the previous stages, such as colors and textures.

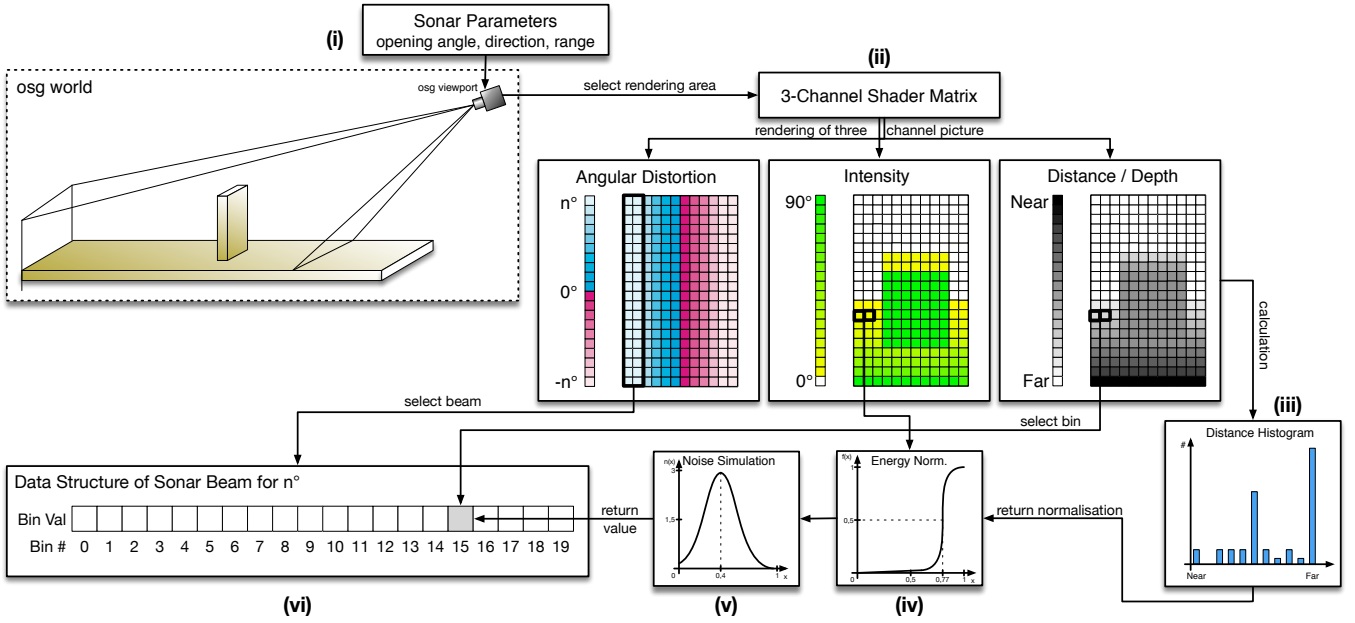


Figure 4: A graphical overview of the imaging sonar simulation process: (i) a virtual camera, specialized as the sonar device, samples the underwater scene; (ii) three parameters are calculated by shader rendering on GPU: **angular distortion**, **intensity** and **depth**; the shader information is split into beam parts, according to the angular distortion values, and the bin depth and the intensity are defined by: distance histogram (iii) and energy normalization (iv), respectively; (v) the speckle noise is applied to the final sonar data; (vi) and the simulated acoustic data is presented as Rock's data type.

221 In our work, the underwater scenes are sampled by a virtual
222 camera (frame-by-frame), whose optical axis is aligned with the
223 intended viewing **direction**, the coverage **range** and the **open-**
224 **ing angle** of the simulated sonar device (see Fig. 4(i)). To sim-
225 ulate the sonar imaging by using virtual camera frames, three
226 parameters are computed in fragment and vertex shaders, dur-
227 ing the rendering pipeline. This way, we are able to use the
228 precomputed geometric information during the image rasteri-
229 zation process on GPU. The three parameters to simulate the
230 sonar using a virtual camera are, as illustrated in Fig. 4(ii):

- **Distance / Depth** is the camera focal length, calculated by the Euclidean distance to the object surface point. **To avoid precision limitation, we used the native GLSL 32-bit floating-point depth buffer;**
- **Intensity** presents the echo reflection energy based on object surface normal angle up to the camera;
- **Angular distortion** is the angle formed from the camera center column up to the camera boundary column, for both directions. **As the sonar's opening angle has a limit of 180 degrees, a 8-bit channel suffices to represent the sonar operation.**

242 All the three parameters in the shader matrix are normalized
243 into the interval [0,1]. For the intensity parameter, zero means
244 no energy and one means maximum echo energy; for depth,
245 the minimum value denotes a close object, while the maximum
246 value represents a far one, limited by the sonar maximum range;
247 angle distortion is zero in image center column, and increases
248 for both borders to present the half value of horizontal field of
249 view.

250 In real world sensing, surfaces usually present irregularities
251 and different reflectance values. To render irregularities in a vir-
252 tual scene (see Fig. 5), the intensity values can also be defined
253 by **normal maps** and material property information. **Normal**
254 **mapping** is a perturbation rendering technique to simulate wrin-
255 kles and dents on the object surface by passing **textures**, mod-
256 ifying the normal directions on shaders. This approach con-
257 sumes less computational resources for the same level of detail,
258 compared with the displacement mapping technique, because
259 the geometry remains unchanged. Since **normal maps** are built
260 in tangent space, interpolating the normal vertex and the tex-
261 ture, tangent, bi-tangent and normal (TBN) matrices are com-
262 puted to convert the normal values into the world space. The
263 reflectance allows to properly describe the intensity received
264 back from observable objects in shader processing, according
265 to their material properties. For instance, aluminum has more re-
266 flectivity than wood and plastic. When an object has its re-
267 flectivity property defined, the reflectance value ρ is passed to
268 the fragment shader and processed **on GPU**. So the final pixel
269 **intensity** represents the product of its normal value by the re-
270 flectance value ρ (see Fig. 6). At the end of sonar rendering
271 step, the shader provides a 3-channel matrix composed by in-
272 tensity, depth and angular distortion parameters.

273 3.3. Simulating sonar device operation

274 The **3-channel** shader matrix is used to compute the corre-
275 sponding acoustic representation. Since the angular distortion
276 is radially spaced over the horizontal field-of-view, where all
277 pixels in the same column have the same angle value, the first
278 step is to split the image into a number of beam parts. Each
279 angular distortion column is correlated with a respective beam

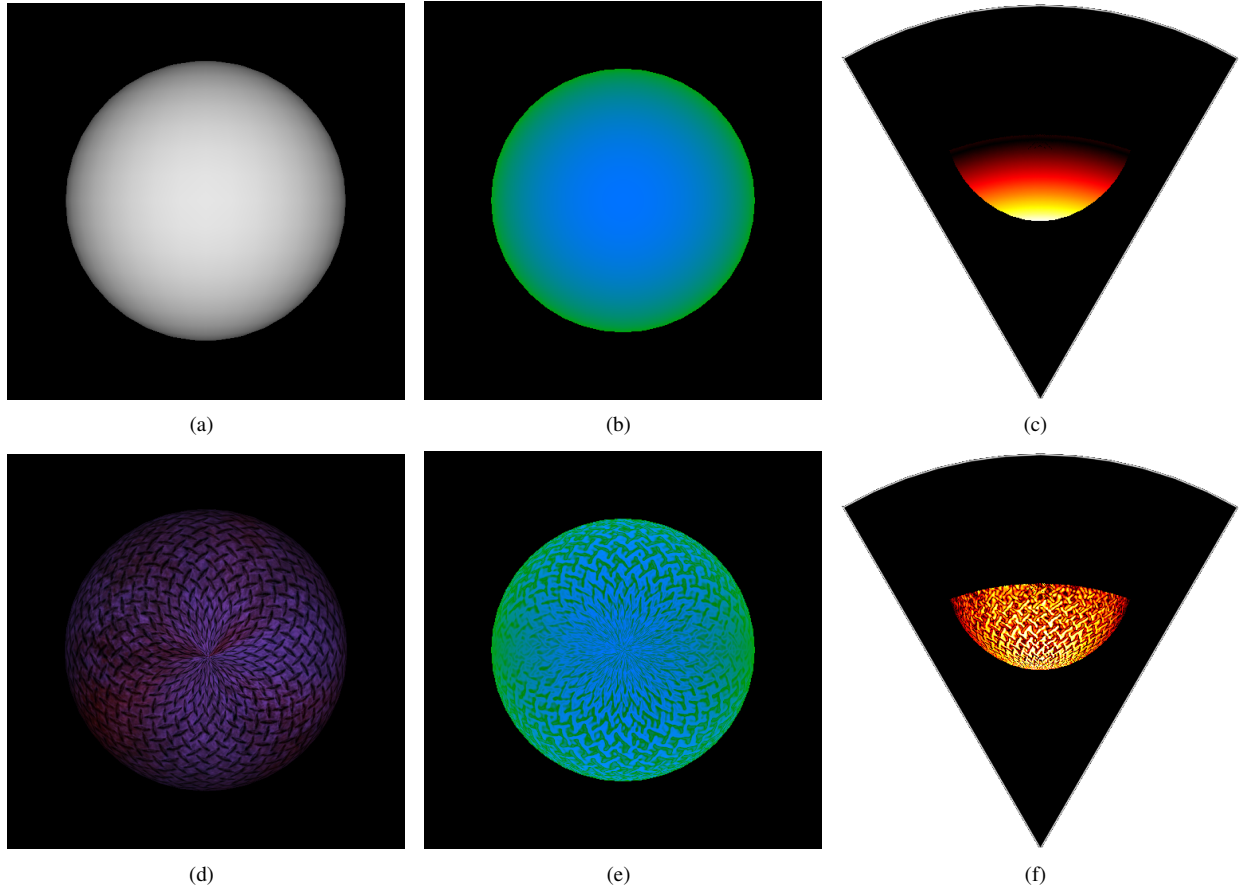


Figure 5: Example of shader rendering with [normal mapping](#): A sphere without (a) and with texture (d); respective shader image representations of the spheres in (b) and (e), where the blue area represents the intensity parameter, while the green area represents the depth parameter. The final acoustic images are depicted in (c) and (f). By using [normal mapping](#) technique, the textures changes the normal directions, and the sonar image details the appearance of object surface, like in real world sensing.

vector, according to sonar bearings, as illustrated in Fig. 4(vi). [One beam represents one or more columns](#). Each beamed sub-image is converted into bin intensities using the depth and intensity [shader matrix parameters](#). In a real imaging sonar, the echo measured back is sampled over time and the bin number is proportional to the sensor range. In other words, the initial bins represent the closest distances, while the latest bins are the farthest ones. Therefore a distance histogram (see Fig. 4(iii)) is computed and evaluated in order to group the sub-image pixels with the respective bins, according to the depth [shader matrix parameter](#). The distance histogram is used to calculate the accumulated intensity of each bin.

Due to the acoustic beam spreading and absorption in the water, the final bins have less echo strength than the first ones, because the energy is twice lost, in the environment. To tackle with that issue, sonar devices use an energy normalization based on time-varying gain for range dependence compensation, which spreads losses in the bins. In our simulation approach, the accumulated intensity in each bin (see Fig. 4(iv)) is normalized as

$$I_{bin} = \sum_{x=1}^N \frac{1}{N} \times S(i_x), \quad (1)$$

where I_{bin} is the intensity in the bin after energy normalization, x is the pixel location in the shader matrix, N is the distance histogram value (number of pixels) of that bin, $S(i_x)$ is a sigmoid function, and i_x is the intensity value of the pixel x .

[Finally, the sonar image size needs to be big enough to contain all information of the bins. For that, the number of bins involved is directly proportional to the sonar image size.](#)

3.4. Noise model

Imaging sonar systems are disturbed by a multiplicative noise known as speckle, which is caused by coherent processing of backscattered signals from multiple distributed targets. [This effect degrades](#) image quality and visual evaluation. Speckle noise results in constructive and destructive interferences, which are shown as bright and dark dots in the image. The noisy image has been expressed as [21]:

$$y(t) = x(t) \times n(t), \quad (2)$$

where t is the time instant, $y(t)$ is the noised image, $x(t)$ is the free-noise image, $n(t)$ is the speckle noise matrix, and \times symbol defines an element-wise multiplication.

[This type of noise is well-modeled as a Gaussian distribution \(see Fig. 4\(v\)\). The physical explanation is provided by](#)

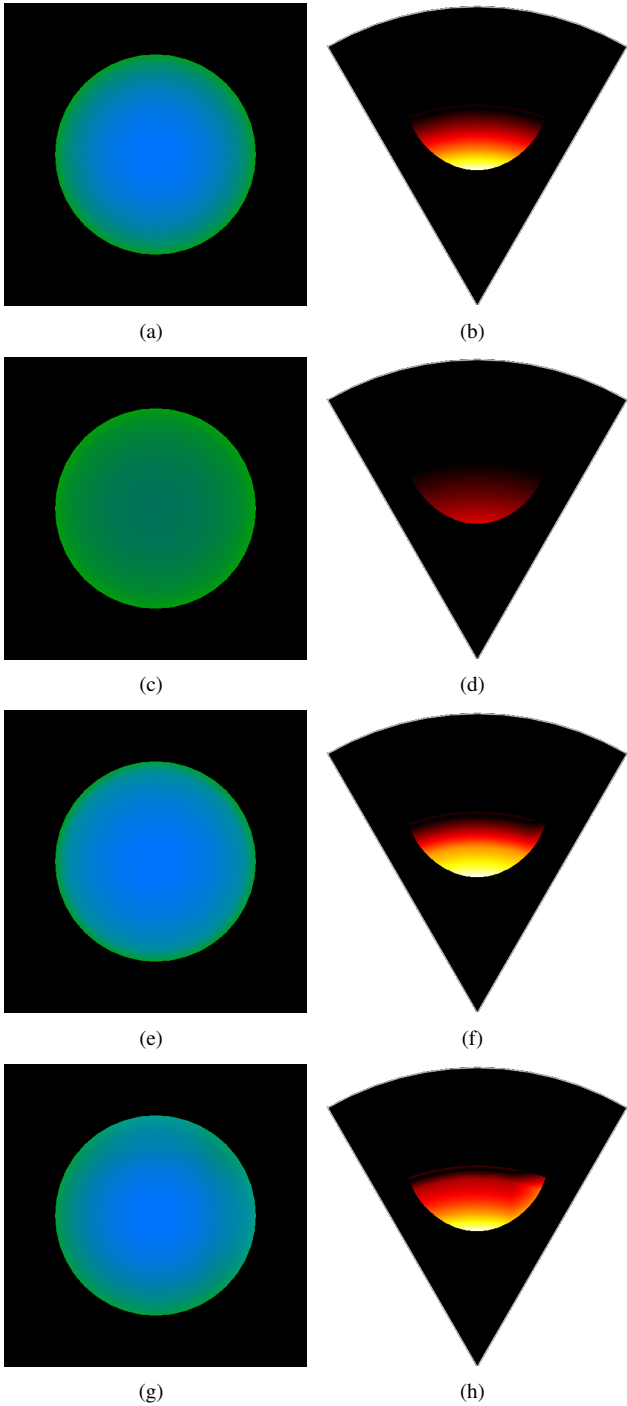


Figure 6: Examples of different reflectance values, ρ , applied in shader image representation of the same target, where blue is the normal channel and green is the depth channel: (a) raw image; (c) $\rho = 0.35$; (e) $\rho = 1.40$; and (g) $\rho = 2.12$. The following acoustic images are presented in (b), (d), (f) and (h).

the central limit theorem, which states that the sum of many independent and identically distributed random variables tends to behave as a Gaussian random variable [22]. A Gaussian distribution is defined by following a non-uniform distribution, skewed towards low values, and applied as speckle noise in the simulated sonar image. This noise simulation is repeated for each virtual acoustic frame.

Table 1: Sonar device configurations used on experimental evaluation.

Device	# of beams	# of bins	Field of view	Down tilt	Motor Step
FLS	256	1000	120° x 20°	20°	-
MSIS	1	500	3° x 35°	0°	1.8°

3.5. Integrating sonar device with Rock

After the imaging sonar simulation process, from the virtual underwater scene to the acoustic representation, the resulting sonar data is encapsulated as Rock's sonar data type and provided as I/O port of a Rock's component, allowing the interaction with other simulated models and applications.

4. Simulation results and experimental analysis

To evaluate our simulator, experiments were conducted by using a 3D model of an AUV equipped with an MSIS and an FLS, studied in different scenarios. The sonar device configurations are summarized in Table 1. In the experimental analysis, as the scene frames are being captured by the sonars, resulting simulated acoustic images are sequentially presented, on-the-fly (see Figs. 7 and 8).

4.1. Experimental evaluation

The virtual FLS from AUV was used to insonify the scenes from three distinct scenarios. A docking station, in parallel with a pipeline on the seabed, composes **the first scenario** (see Fig. 7(a)); the target surface is well-defined in the simulated acoustic frame (see Fig. 7(b)), even as the shadows and speckle noise; given that the docking station is metal-made, the texture and reflectivity were set, such that a higher intensity shape was resulted in comparison with the other targets. **The second scenario** presents the vehicle in front of a manifold model in a non-uniform seabed (see Fig. 7(c)); the target model was insonified to generate the sonar frame from the underwater scene (see Fig. 7(d)); the frontal face of the target, as well the portion of the seabed and the degraded data by noise, are clearly visible in the FLS image; also, a long acoustic shadow is formed behind the manifold, occluding part of the scene. **The third scenario** contains a sub-sea isolation valve (SSIV) structure, connected to a pipeline in the bottom (see Fig. 7(e)); the simulated acoustic image, depicted in Fig. 7(f), also present shadows, material properties and speckle noise effects. Due to sensor configuration and robot position, the initial bins usually present a blind region in the three simulated scenes, caused by absence of objects at lower ranges, similar to real sonar images. Also, the brightness of sea-floor decreases, as the sea-floor is farther from sonar, because of the normal orientation of the surface.

The MSIS was also simulated in three different experiments. The robot in a big textured tank composes **the first scene** (see Fig. 8(a)); similar to the first scenario of FLS experiment, the reflectivity and texture were set to the target; the rotation of the sonar head position, by a complete 360° scanning, produced

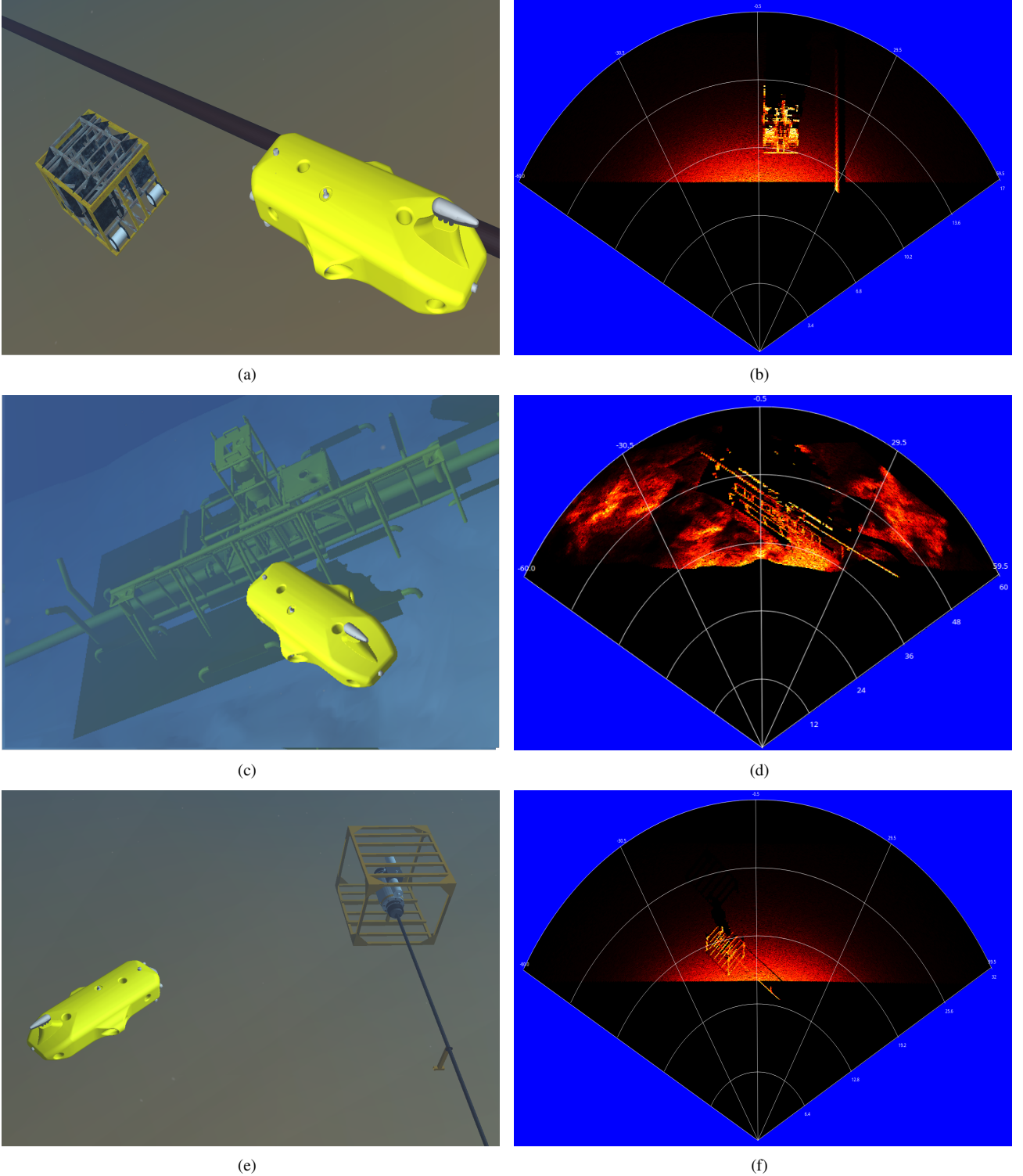


Figure 7: Forward-looking sonar simulation experiments: (a), (c) and (e) present the virtual underwater trials, while (b), (d) and (f) are the following acoustic representations of each scenario, respectively.

373 the acoustic frame of tank walls (see Fig. 8(b)). **The second**
 374 **scene** involves the vehicle's movement during the data acqui-
 375 sition process; the scene contains a grid around the AUV (see
 376 Fig. 8(c)), captured by an MSIS in the front of the AUV; this
 377 trial induces a distortion in the final acoustic frame, because the

378 relative sensor position with respect to the surrounding object
 379 changes, as the sonar image is being built (see Fig. 8(d)); in
 380 this case, the robot rotates 20° left during the scanning. **The**
 381 **last scene** presents the AUV over oil and gas structures on the
 382 sea bottom (see Fig. 8(e)); using an MSIS located in the back

383 of the AUV, with a vertical orientation, the scene was scanned
384 to produce the acoustic visualization; as illustrated in Fig. 8(f),
385 object surfaces present clear definition in the slice scanning of
386 the sea-floor.

387 All the experimental scenarios provided enough variabil-
388 ity of specific phenomena usually found in real sonar images,
389 such as acoustic shadows, noise interference, surface irregular-
390 ities and properties, distortion during the acquisition process
391 and gradient of acoustic intensities. However, the speckle noise
392 application is restricted to regions with acoustic intensity, as
393 shown in Figs. 7(f) and 8(b). This fact is due to our sonar model
394 be multiplicative (defined in Eq. 2). In real sonar images, the
395 noise also granulates the shadows and blind regions. The sonar
396 simulator can be improved by inserting an additive noise to our
397 model. **The impact of additive noise on the image is more se-
398 vere than that of multiplicative, and we decided to collect more
399 data before include this type of noise in our simulator.** A sec-
400 ond feature missing in simulated acoustic images are the ghost
401 effects caused by reverberation. This lacking part can be ad-
402 dressed by implementation of a multi-path propagation model
403 as found in [23].

404 4.2. Computational time

405 Performance evaluation of the simulator was determined by
406 considering the suitability to run real-time applications. The
407 experiments were performed on a laptop with Ubuntu 16.04
408 64 bits, Intel Core i7 3540M processor running at 3 GHz with
409 16GB DDR3 RAM memory and NVIDIA NVS 5200M video
410 card.

411 The elapsed time of each sonar data is stored to compute the
412 average time, standard deviation and frame rate metrics, after
413 500 iterations, as summarized in Tables 2 and 3. After chang-
414 ing the device parameters, such as number of bins, number of
415 beams and field of view, the proposed approach generated the
416 sonar frames with a high frame rate, for both sonar types. Given
417 the Tritech Gemini 720i, a real forward-looking sonar sensor,
418 with a field of view of 120° by 20° and 256 beams, presents a
419 maximum update rate of 15 frames per second, the results allow
420 the use of the sonar simulator for real-time applications. Also,
421 the MSIS data built by the simulator is able to complete a 360°
422 scan sufficiently fast in comparison with a real sonar as Tritech
423 Micron DST. Moreover, for the FLS device, these rates are su-
424 perior to the rates lists by DeMarco *et al* [4] (330ms) and Saç
425 *et al* [3] (2.5min). For MSIS type, to the best of our knowledge,
426 **there is no previous work for comparison.**

427 According to previous results, since the number of bins is
428 directly proportional to sonar image resolution, as explained in
429 Section 3.3, this is also correlated with the computational time.
430 When the number of bins increases, the simulator will have a
431 bigger scene frame to compute, and generate the sonar data.

432 5. Conclusion and future work

433 A GPU-based approach for imaging sonar simulation is pre-
434 sented here. The same model was able to reproduce the oper-
435 ation mode of two different types of sonar devices (FLS and

436 MSIS) over different scenarios. The real sonar image singulari-
437 ties, such as multiplicative noise, surface properties and acous-
438 tic shadows are addressed and represented in the simulated frames.
439 Specially for the shadows, the acoustic representation can present
440 information as useful as the insonified object. Considering the
441 qualitative results, **the sonar simulator can be used** by feature
442 detection algorithms, based on corners, lines and shapes. Also,
443 the computation time to build one sonar frame was calculated
444 using different device settings. The vertex and fragment pro-
445 cessing during the underwater scene rendering accelerates the
446 sonar image building, and the metrics, such as the average time,
447 demonstrated that the performance is much close to real imag-
448 ing devices. These results allowed the use of this imaging sonar
449 simulator by real-time applications, such as obstacle detection
450 and avoidance, and object tracking. Finally, the reverberation
451 effect is still missing on our simulator to perform a more re-
452 alistic sensing. The future inclusion of this phenomenon will
453 probably change the reflected intensity model and the compu-
454 tation time must be considered again. Next steps will focus
455 on **to expand the underwater acoustic characteristics, such as
456 additive noise and reverberation, and** qualitative and computa-
457 tion-efficiency evaluations with other imaging sonar simulators
458 and real images.

459 **Recently we had the opportunity to record a lot of imaging
460 sonar data during tests. The target structures we were operat-
461 ing on, have been made by us ourselves and we have detailed
462 models in simulation (see Figs. 7(f) and 9). We therefore plan
463 to use this data in the next months to analyse the quality of the
464 simulation.**

465 References

- 466 [1] Bell JM. Application of optical ray tracing techniques to the simulation
467 of sonar images. *Optical Engineering* 1997;36(6):1806–13.
- 468 [2] Coiras E, Groen J. Simulation and 3d reconstruction of side-looking sonar
469 images. In: Silva S, editor. *Advances in Sonar Technology*; chap. 1. In-
470 Tech; 2009, p. 1–15.
- 471 [3] Saç H, Leblebicioğlu K, Bozdağı Akar G. 2d high-frequency
472 forward-looking sonar simulator based on continuous surfaces ap-
473 proach. *Turkish Journal of Electrical Engineering and Computer Sciences*
474 2015;23(1):2289–303.
- 475 [4] DeMarco K, West M, Howard A. A computationally-efficient 2d imag-
476 ing sonar model for underwater robotics simulations in Gazebo. In:
477 *MTS/IEEE OCEANS Conference*. 2015, p. 1–8.
- 478 [5] Gu J, Joe H, Yu SC. Development of image sonar simulator for under-
479 water object recognition. In: *MTS/IEEE OCEANS Conference*. 2013, p.
480 1–6.
- 481 [6] Kwak S, Ji Y, Yamashita A, Asama H. Development of acoustic camera-
482 imaging simulator based on novel model. In: *IEEE International Con-
483 ference on Environment and Electrical Engineering (EEEIC)*. 2015, p.
484 1719–24.
- 485 [7] Guériot D, Sintes C. Forward looking sonar data simulation through tube
486 tracing. In: *MTS/IEEE OCEANS Conference*. 2010, p. 1–6.
- 487 [8] Quigley M, Conley K, Gerkey BP, Faust J, Foote T, Leibs J, et al. ROS:
488 an open-source robot operating system. In: *Workshop on Open Source
489 Software*, held at *IEEE International Conference on Robotics and Auto-
490 mation (ICRA)*. 2009, p. 1–6.
- 491 [9] Hurtós N. Forward-looking sonar mosaicing for underwater environments.
492 Ph.D. thesis; Universitat de Girona; 2014.
- 493 [10] Abbot J, Thurstone F. Acoustic speckle: theory and experimental analy-
494 sis. *Ultrasonic Imaging* 1979;1(4):303–24.
- 495 [11] Ganesan V, Chitre M, Brekke E. Robust underwater obstacle detection
496 and collision avoidance. *Autonomous Robots* 2015;40(7):1–21.

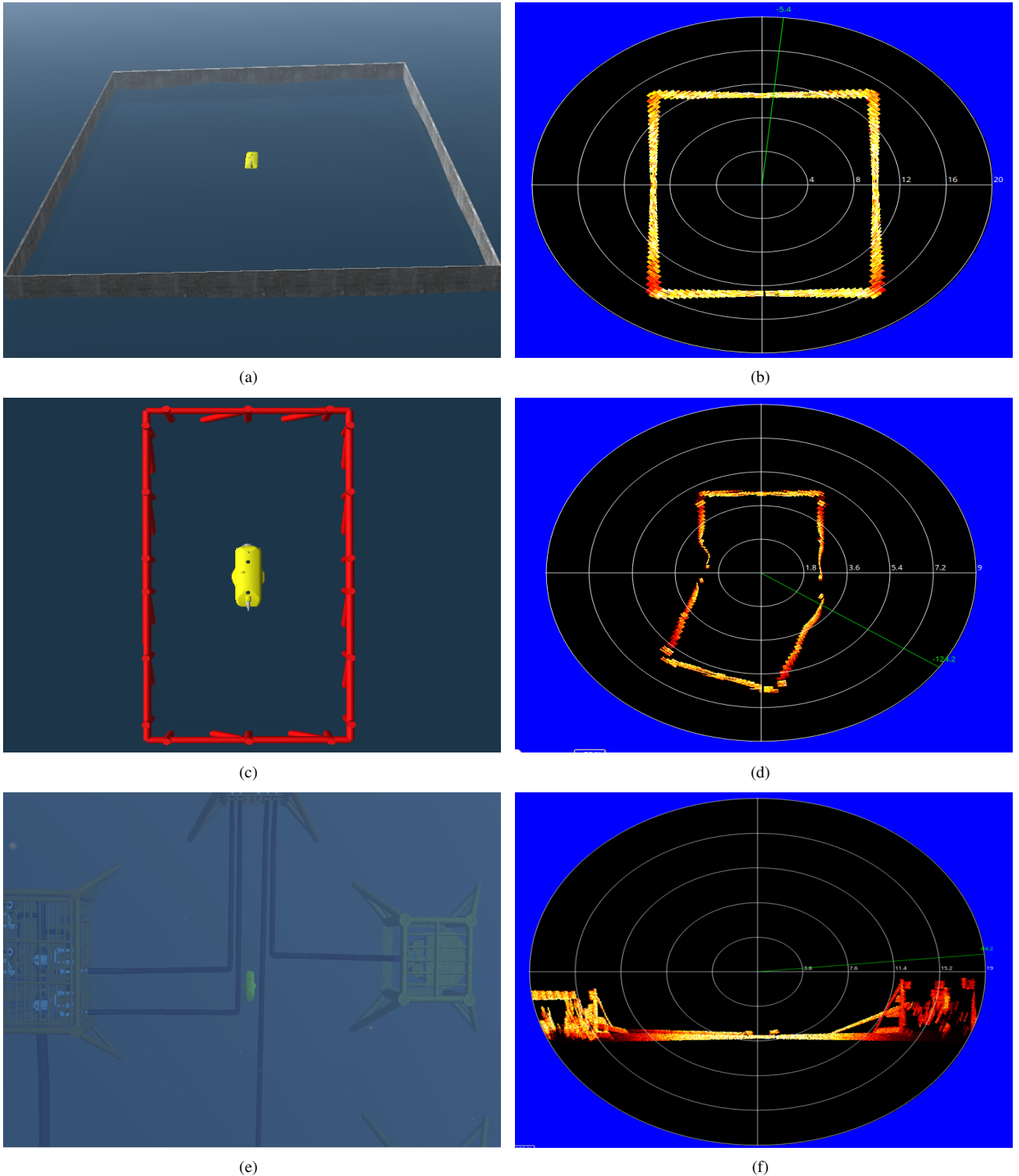


Figure 8: Experiments using mechanical scanning imaging sonar in three different scenarios (a), (c) and (e), and the respective processed simulated frames in horizontal axis in (b) and (d), and vertical axis in (f).

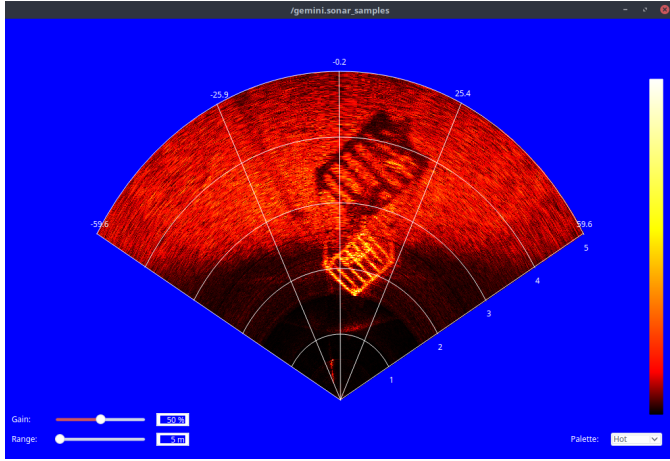
- 497 [12] Ribas D, Ridao P, Neira J. Underwater SLAM for structured environments using an imaging sonar. Springer-Verlag Berlin Heidelberg; 2010.
 498
 499 [13] Fallon MF, Folkesson J, McClelland H, Leonard JJ. Relocating underwater features autonomously using sonar-based SLAM. *Journal of Ocean Engineering* 2013;38(3):500–13.
 500
 501 [14] Liu L, Xu W, Bian H. A LBF-associated contour tracking method for
 502 underwater targets tracking. In: MTS/IEEE OCEANS Conference. 2016, p. 1–5.
 503
 504 [15] Huang TA, Kaess M. Towards acoustic structure from motion for imaging sonar. In: IEEE/RSJ International Conference on Intelligent Robots and Systems (IROS). 2015, p. 758–65.
 505
 506 [16] Bradski G. The opencv library. *Doctor Dobbs Journal* 2000;25(11):120–
 507

Table 2: Processing time to generate forward-looking sonar frames with different parameters.

# of samples	# of beams	# of bins	Field of view	Average time (ms)	Std dev (ms)	Frame rate (fps)
500	128	500	120° x 20°	54.7	3.7	18.3
500	128	1000	120° x 20°	72.3	8.9	13.8
500	256	500	120° x 20°	198.7	17.1	5.0
500	256	1000	120° x 20°	218.2	11.9	4.6
500	128	500	90° x 15°	77.4	11.8	12.9
500	128	1000	90° x 15°	94.6	10.2	10.6
500	256	500	90° x 15°	260.8	18.5	3.8
500	256	1000	90° x 15°	268.7	16.7	3.7

Table 3: Processing time to generate mechanical scanning imaging sonar samples with different parameters.

# of samples	# of bins	Field of view	Average time (ms)	Std dev (ms)	Frame rate (fps)
500	500	3° x 35°	8.8	0.7	113.4
500	1000	3° x 35°	34.5	1.6	29.0
500	500	2° x 20°	10.3	0.6	96.7
500	1000	2° x 20°	41.7	3.7	24.0



Carleton University; 2015.

Figure 9: Image of a Tritech Gemini 720i Imaging Sonar of a mock-up of a sub-sea structure.

- 509 6.
- 510 [17] Watanabe T, Neves G, Cerqueira R, Trocoli T, Reis M, Joyeux S, et al.
511 The Rock-Gazebo integration and a real-time AUV simulation. In: IEEE
512 Latin American Robotics Symposium (LARS). 2015, p. 132–8.
- 513 [18] SDF. <http://sdformat.org/>; 2017. Accessed: 2017-04-23.
- 514 [19] Soetens P, Bruyninckx H. Realtime hybrid task-based control for robots
515 and machine tools. In: IEEE International Conference on Robotics and
516 Automation (ICRA). 2005, p. 260–5.
- 517 [20] Rost RJ, Licea-Kane B, Ginsburg D, Kessenich JM, Lichtenbelt B, Malan
518 H, et al. OpenGL shading language. 3rd ed.; Addison-Wesley Profes-
519 sional; 2009.
- 520 [21] Lee J. Digital image enhancement and noise filtering by use of local sta-
521 tistics. IEEE Transactions on Pattern Analysis and Machine Intelligence
522 1980;2(2):165–8.
- 523 [22] Papoulis A, Pillai S. Probability, random variables and stochastic pro-
524 cesses. McGraw Hill; 2002.
- 525 [23] Huang J. Simulation and modeling of underwater acoustic communica-
526 tion channels with wide band attenuation and ambient noise. Ph.D. thesis;